

## Supporting Information

### Coupling the Chemical Reactivity of Bimetallic Surfaces to the Orientations of Liquid Crystals

*Tibor Szilvási<sup>#</sup>, Huaizhe Yu<sup>#</sup>, Jake I. Gold, Nanqi Bao, Trenton J. Wolter, Robert J. Twieg, Nicholas L. Abbott<sup>\*</sup>, Manos Mavrikakis<sup>\*</sup>*

#### Significance of the Study

Our paper represents a conceptual advance in the design of stimuli-responsive soft materials because it is the first to report that the chemical reactivity of bimetallic interfaces, which have been widely explored in the context of their reactivity for chemical catalysis, can be coupled to soft materials to enable chemically-responsive soft materials. This connection - soft materials + reactivity of bimetallic surfaces - is a conceptual advance as it provides an entry point to a new set of materials designs that allow the presence of specific chemical species to trigger a response in a soft material. The field of catalysis/reactivity of bimetallics is enormous, yet the field of catalysis/reactivity of bimetallics has not previously been connected to the design of responsive soft material systems.

#### Computational Details

Density Functional Theory (DFT) calculations were carried out using the Vienna Ab initio Simulation Package (VASP) code.<sup>1,2</sup> Projector augmented wave potentials were used to describe the electron-ion interactions,<sup>3,4</sup> and the exchange-correlation functional was described by the generalized gradient approximation (GGA-PBE).<sup>5</sup> Grimme's D3 empirical dispersion correction scheme with zero damping were employed in all calculations.<sup>6</sup> Electronic wave function was expanded using plane waves with an energy cutoff of 400 eV. The Brillouin zone (BZ) was sampled using  $(4 \times 4 \times 1)$ ,  $(3 \times 3 \times 1)$ , and  $(2 \times 3 \times 1)$   $\Gamma$ -centered Monkhorst-Pack k-point mesh<sup>7</sup> in the case of  $(3 \times 3)$ ,  $(4 \times 4)$ , and  $(6 \times 4)$  unit cell calculations, respectively. In all calculations, the Methfessel-Paxton smearing method<sup>8</sup> was used with 0.1 eV smearing. Structures were relaxed until the Hellmann-Feynman forces acting on each atom were less than  $0.02 \text{ eV \AA}^{-1}$ .

The calculated lattice constant of Au ( $4.12 \text{ \AA}$ ) and Pd ( $3.90 \text{ \AA}$ ) is in good agreement with the experimental value of  $4.08 \text{ \AA}$  and  $3.89 \text{ \AA}$ , respectively.<sup>9</sup> The gold and palladium surfaces were modeled using the most stable (111) facet with a four-layer slab. The bottom two layers of the slab were fixed in their bulk positions, while the two top layers of Au atoms were relaxed in all calculations. For bimetallic surfaces, a five-layer slab was used, and the three top layers were relaxed. In all calculations, we applied a vacuum layer of at least  $15 \text{ \AA}$  between periodic images even in case of the perpendicular orientation of PhPhCN adsorbate, which was used as surrogate of 4'-n-pentyl-4-biphenylcarbonitrile (5CB)<sup>10</sup>. Dipole correction was used to eliminate residual interaction between images through the vacuum layer<sup>11</sup>. The binding energy (BE) of an adsorbate is defined by  $BE = E_{\text{total}} - E_{\text{substrate}} - E_{\text{gas phase adsorbate}}$  where  $E_{\text{total}}$  is the total energy of the entire adsorbate-slab system,  $E_{\text{substrate}}$  is the total energy of the clean slab, and  $E_{\text{gas-phase adsorbate}}$  is the total energy of the isolated adsorbate in the gas phase. By this definition, a more negative BE value reflects a stronger binding to the surface. Binding free energy (BFE) is defined

analogously. To compare binding in different orientations calculated in various unit cells and coverages, we introduce the descriptor total binding energy normalized per unit area (BE/A) defined as a sum of the BE of all adsorbates present in the unit cell ( $\sum BE$ ) and divided by the area of the unit cell (A):  $BE/A = \sum BE/A$ . By this definition, a more negative BE/A value reflects a stronger overall binding of the adsorbate layer to the surface. Total binding free energy normalized per unit area (BFE/A) is defined accordingly. The calculation of BFE/A was chosen over the BFE of a single molecule because, in general, a liquid at the solid-liquid interface will prefer molecular organizations that minimize the total free energy at the surface, not the free energy of a given number of molecules in the surface layer. This free energy minimization criterion is better reflected by the total BFE of the molecules representing the liquid phase on the surface than the BFE of one molecule. Normalization per unit area is necessary to compare structures that occupy significantly different surface areas and to find which structure minimizes the total free energy at the interface. We show that BFE/A provides meaningful insights by showing the large variation in the stability of perpendicular orientation as a function Pd coverage in the surface and by showing that perpendicular orientation is less favorable than parallel orientation at low Pd coverage (Figure 1a). Both of these predictions are in agreement with experimental findings.

## Experimental Details

**Materials.** Palladium (II) chloride, hydrochloric acid (37%), sulfuric acid (98%) and 4'-octyl-4-biphenylcarbonitrile (8CB) were purchased from Sigma-Aldrich (Milwaukee, WI). Titanium (99.999%) and gold (99.999%) were purchased from Advanced Materials (Spring Valley, NY). Fischer's Finest glass slides were purchased from Fischer Scientific (Pittsburgh, PA). Absolute ethanol (anhydrous, 200 proof) was purchased from Pharmco-AAPER (Brookfield, CT). 5CB was purchased from Jiangsu Hecheng Advanced Materials Co., Ltd (Jiangsu, China). Silicon wafers were purchased from Silicon Sense (Nashua, NH). 10 ppm  $Cl_2$  balanced with  $N_2$  (purity of  $Cl_2$  is 99.9% and purity of  $N_2$  is 99.999%) and  $N_2$  (99.999% purity) were obtained from Airgas (Radnor Township, PA) and used as received. All chemicals and solvents were of analytical reagent grade and were used as received without any further purification. Fiber spacers with 5  $\mu m$ -diameter were purchased from EM industries, Inc (Hawthorne, NY). All aqueous solutions used in this study were made by deionized water possessing a resistivity of at least 18.2 M $\Omega$ .

**Cleaning of glass substrates.** Glass microscope slides were cleaned according to published procedures<sup>12</sup> using an acidic piranha solution [70:30 (% v/v)  $H_2SO_4$  (70%): $H_2O_2$  (30%)]. Piranha is extremely corrosive, potentially explosive and should not be exposed to organic material under any circumstances.<sup>13</sup> Briefly, the glass slides were immersed in a piranha bath at 60-80 °C for at least 1 h and then rinsed in running deionized water for 2-3 mins. The slides were then immersed in basic piranha solution [70:30 (%v/v) KOH (45%): $H_2O_2$  (30%)] and heated to between 60 and 80 °C for at least 1 h. Finally, the slides were rinsed sequentially in deionized water, ethanol, and then dried under a stream of nitrogen. The clean slides were stored in a vacuum oven at 110 °C overnight. All other glassware was cleaned prior to use.

**Preparation of Gold Substrates for Polarized Light Microscopy.** Semitransparent films of gold with thicknesses of 200 Å were deposited onto piranha-cleaned glass slides mounted on a fixed holder within an electron-beam evaporator (VEC-3000-C manufactured by Tekvac Industries, Brentwood, NY). A layer of titanium (thickness 20 Å) was used to promote adhesion between the glass microscope slides and the films of gold. The rates of deposition of both gold and titanium were 0.2 Å/s. The pressure in the evaporator was maintained below  $3 \times 10^{-6}$  Torr before and during the deposition. Predominant crystallographic face of vacuum-deposited polycrystalline Au substrate is Au(111).<sup>14</sup>

**Preparation of Gold Substrates for X-Ray Photoelectron and Infrared Spectroscopy.** Substrates used for the infrared (IR) and X-ray photoelectron spectroscopy (XPS) were prepared by sequential deposition of 100 Å of titanium and 1000 Å of gold onto silicon wafers. The gold-coated silicon wafers were then cut to 15 mm × 30 mm pieces and cleaned under a gaseous stream of nitrogen.

**Preparation of Palladium Surfaces.** Electrochemical experiments were performed using an AFCBP1 bipotentiostat from Pine Instruments (Grove City, PA). The electrochemical cell was arranged in a standard three-electrode configuration using a gold film (working electrode), a platinum wire mesh (counter electrode), and a silver chloride electrode (reference electrode, BASi, West Lafayette, IN). Palladium overlayers on the gold were prepared by electrodeposition from a 0.1 M H<sub>2</sub>SO<sub>4</sub> + 0.1 mM H<sub>2</sub>PdCl<sub>4</sub> at 570 mV vs. Ag/AgCl for submonolayers of Pd or at 440 mV vs. Ag/AgCl for multilayers of Pd.<sup>15</sup> The amount of Pd deposited onto the Au surfaces was controlled by the charge passed: one monolayer (ML) equivalent was defined as 440 μC/cm<sup>2</sup> for Pd deposition on Au(111). After Pd deposition, the electrode was removed from the electrochemical cell, and rinsed 2 minutes with flowing Milli-Q water.

**Ellipsometry.** The optical thicknesses of films of 8CB deposited by spin-coating onto gold films were measured using a Gaertner LSE ellipsometer at a wavelength of 632.8 nm and an angle of incidence of 70°. The deposited films were assumed to have refractive indices of  $n = 1.6$ .<sup>16</sup>

**Preparation of Micrometer-Thick Films of LC with Free Surfaces.** 20 μm-thick copper-coated transmission electron microscopy (TEM) grids (Electron Microscopy Sciences, Hatfield, PA) were placed onto the surfaces of semitransparent gold films. The TEM grids possessed square pores with lateral dimensions of 285 μm. 0.2 μL of 5CB was deposited into each TEM grid using a glass capillary. The excess LC was removed from the grid by wicking the LC into an empty capillary tube.

**Anchoring Transitions Induced by Cl<sub>2</sub>.** LC samples hosted within TEM grids supported on gold films were exposed to a stream of nitrogen containing Cl<sub>2</sub> within a flow cell that was constructed to direct the gaseous flow across the LC samples while permitting observation of the samples through a polarized-light microscope (CH40, Olympus, Melville, NY). A detailed description of the flow cell can be found in a prior publication.<sup>17</sup> The stream of gas containing Cl<sub>2</sub> was generated from a certified cylinder of 10 ppm Cl<sub>2</sub> in nitrogen and diluted using nitrogen to 1 ppm (see Materials for purity). The flow rate of gas through the flow cell was controlled to be 1000 mL/min using a series of rotameters (Aalborg Instruments & Controls, Inc., Orangeburg, NY).

**Measurement of Optical Retardance.** The optical retardance ( $\Delta\gamma$ ) values of LC films were measured by comparing the interference colors of LC samples (imaged between crossed polarizers using white light) to those found in Michel-Levy chart. The tilt angle ( $\theta$ , measured from the surface normal) was calculated using

$$\Delta\gamma \approx \int_0^d \left( \frac{n_o n_e}{\sqrt{n_o^2 \sin^2 \left( \left(1 - \frac{z}{d}\right) \theta_{bottom} \right) + n_e^2 \cos^2 \left( \left(1 - \frac{z}{d}\right) \theta_{bottom} \right)}} - n_o \right) dz$$

in which  $n_o$  and  $n_e$  are the indices of refraction perpendicular and parallel to the optical axis of the LC, respectively. The solution of this equation yields  $\theta_{bottom}$ , the orientation of LC on the bottom substrate (measured from surface normal).

**X-ray Photoelectron Spectroscopy (XPS).** Samples were analyzed using a Scienta Omicron ESCA-2SR with operating pressure  $\sim 1 \times 10^{-9}$  Torr. Monochromatic Al K $\alpha$  x rays (1486.6 eV) were used and photoelectrons were collected from a 5 mm diameter analysis area. Photoelectrons were collected at a 0° emission angle with a source to analyzer angle of 54.7°.

A pass energy of 200 eV was used for wide/survey scans, and 50 eV was used for high resolution scans. The samples were conductive and did not require charge neutralization. Survey scans were collected at 100ms dwell times, with high resolution scans collected at 300ms for Pd, 100ms for C, 300ms for O, 300ms for Cl, and 100ms for Au. All XPS results presented in this paper were analyzed by CasaXPS software. The XPS line shape was assumed to be a Gaussian-Lorentzian function for the oxygen component and an asymmetrical Voigt functions for Pd component, which was employed successfully in previous studies.<sup>18,19</sup>

**Fourier Transformed Polarization-Modulation Infrared Reflectance Absorbance Spectroscopy (PM-IRRAS).** For IR studies, 100  $\mu$ L of 2 mM 8CB in ethanol was spin coated onto each gold-coated silicon wafer at 3000 rpm for 30s. IR spectra of 8CB films deposited onto Pd and Au-coated silicon wafers were obtained using a Nicolet Magna-IR 860 FT-IR spectrometer with a photoelastic modulator (PEM-90, Hinds Instruments, Hillsboro, OR), synchronous sampling demodulator (SSD-100, GWC Technologies, Madison, WI), and a liquid N<sub>2</sub>-cooled mercury cadmium telluride (MCT) detector. All spectra (1000-4000 cm<sup>-1</sup>) were recorded at an incident angle of 83° with the modulation centered at either 2200 cm<sup>-1</sup> or 1500 cm<sup>-1</sup>. For each sample, 1000 scans were taken at a resolution of 4 cm<sup>-1</sup>. Data were collected as differential reflectance vs wavenumber, and spectra were normalized and converted to absorbance units via the method outlined in Frey et al.<sup>20</sup>

## Computational Models

We developed five slab models to understand the orientational behavior of 5CB on Au and PdAu bimetallic surfaces that can be formed using electrochemical Pd deposition on Au films. To evaluate the effect of Pd and alloying with Au, we also use an Au(111) model surface (Figure S1) for comparison. Because previous heterogeneous catalysis and surface science studies suggest that several nanometer of metal layers are sufficient to obtain bulk metal behavior independent from the effect of the underlying substrate, we use a four-layer Pd(111) slab model (Figure S1) to describe thick Pd layers deposited on Au films. Further, we constructed three PdAu alloy slabs: having 1 monolayer (ML) Pd on Au(111), 1/8 ML Pd substituted in Au(111), and 1/16 ML Pd substituted in Au(111) (Figure S1). These models represent two extremes of PdAu alloys. 1/8 ML and 1/16 ML Pd on Au(111) indicate the atomic-scale limit of single atom alloying where single Pd atoms are incorporated into the Au film. Conversely, 1 ML Pd on Au(111) represents the complete Pd monolayer coverage of a Au film. We emphasize here the fundamental difference between 1 ML Pd on Au and multiple ML Pd on Au. 1 ML Pd directly interacts with Au atoms (ligand effect), and its lattice constant is that of the substrate Au (expansive strain compared to pure Pd). For multiple nanometer of Pd both strain and ligand effects induced by Au become negligible, and in that case the pure Pd(111) model is sufficient.

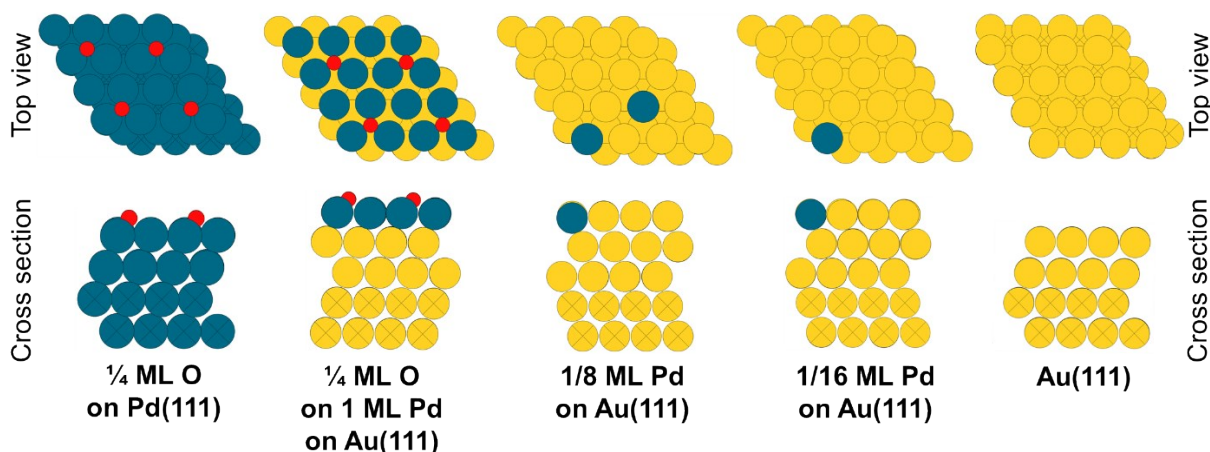


**Figure S1.** Top view (top row) and cross section (bottom row) for computational models under experimentally relevant conditions (1 atm air, 298 K), from left to right:  $\frac{1}{4}$  ML O-precovered Pd(111),  $\frac{1}{4}$  ML O-precovered 1 ML Pd on Au(111),  $\frac{1}{8}$  ML Pd on Au(111),  $\frac{1}{16}$  ML Pd on Au(111), and Au(111). Red, cyan, and yellow colors indicate O, Pd, and Au atoms, respectively. Crossed atoms were not allowed to relax during geometry optimization.

We assess the model surfaces with respect to experimentally relevant conditions to evaluate possible adsorbed states. Specifically, we analyze the effect of air on the surfaces and potential bulk alloying of Pd and Au instead of Pd surface segregation.  $O_2$  in air can lead to dissociative adsorption on metal surfaces, depending on the kinetics characterizing the process on a given surface. Previous surface science literature showed that  $O_2$  dissociation on pristine Au(111) is endothermic and kinetically limited at room temperature<sup>21</sup> while pristine Pd(111) can form  $\frac{1}{4}$  ML O coverage upon exposure to  $O_2$ <sup>22</sup>. Previous experimental work<sup>23</sup> estimated the  $O_2$  dissociation barrier to be 35 and 33 kJ/mol for 2 ML Pd on Au and 4 ML Pd on Au, respectively. We also calculated  $O_2$  dissociation on Pd(111), 1ML Pd on Au(111) and  $\frac{1}{16}$  ML Pd on Au(111) using climbing image nudged elastic band (CI-NEB) calculations<sup>24</sup> with seven images and the previously described computational settings that provided a barrier of 0.54, 0.55, and 1.10 eV, respectively, which suggested that  $O_2$  dissociation is possible on high Pd coverage surfaces but very difficult in the single atom alloy limit. Additionally, we note that our XPS experiments suggest similar surface coverage of O on Pd-rich surfaces (see experimental section). Based on these results, we decided to use the  $\frac{1}{4}$  ML O pre-covered Pd(111) and  $\frac{1}{4}$  ML O pre-covered 1 ML Pd on Au(111) for the rest of our study instead of the clean surfaces, but no O coverage was modeled for  $\frac{1}{8}$  ML and  $\frac{1}{16}$  ML Pd on Au(111) and pristine Au(111).

We also investigate the potential of bulk alloying between Pd and Au, instead of surface segregation of Pd. We find that, under vacuum, in the  $\frac{1}{16}$  ML Pd on Au(111) model moving a Pd atom into the second layer from the surface is energetically favorable by 0.21 eV (1 eV = 96.5 kJ/mol). However, in the presence of surface adsorbates, Pd is preferentially pulled back to the surface because stronger bonding between the adsorbates and the Pd atoms (compared to Au atoms) gain more energy for the system than the cost of pull the Pd atoms to the Au surface. This is the well-known phenomenon of adsorbate-induced surface segregation<sup>25</sup>. Therefore, we do not consider the Pd into the bulk of Au slabs for the rest of our study. Importantly, our XPS results also support this choice (see experimental section).

### Binding of PhPhCN on Model Surfaces

Using the evaluated computational slab models, we intend to predict the binding of 5CB on PdAu bimetallic surfaces. To simplify the structure of 5CB, we neglect the effect of the aliphatic

tail of 5CB and use PhPhCN as a surrogate molecule. This is a reasonable simplification as aliphatic groups only physisorb to Pd and Au surfaces. Furthermore, previous computational chemistry studies have shown that on Au(111) the binding energy of 5CB and of PhPhCN is identical for perpendicular adsorbed orientation, and that the difference in binding energy between the two molecules and Au(111) for the parallel adsorbed orientation is small ( $<0.1$  eV).<sup>26</sup> To understand the binding of PhPhCN in perpendicular and parallel adsorption orientations, we must compare binding in different unit cells and different coverages. We therefore introduce a descriptor called binding free energy normalized per unit area (BFE/A, see details in computational methods section). Table S1 collects the calculated BFE/A values for different model surfaces. As an advantage of BFE/A, we can also compare the binding of PhPhCN in the *same* orientation in different unit cells and coverages and report the most favorable values only. We find that (4x4) and (6x4) unit cells with  $\frac{1}{4}$  and  $\frac{1}{12}$  coverages provide the most stable BFE/A values for perpendicular and parallel orientations, respectively. The only exception is for the  $\frac{1}{16}$  ML Pd on Au(111) model for which (6x4) unit cell is not possible to define with 1.5 Pd atoms. Instead, we use (4x4) unit cell with  $\frac{1}{16}$  coverage to evaluate the stability of the parallel adsorption mode.

**Table S1.** Calculated binding free energy per unit area (BFE/A) of PhPhCN on various surfaces with orientations parallel or perpendicular to the surface. Most stable orientation for each surface is in bold. All energies are in eV/nm<sup>2</sup>. BFE/A is defined as the total binding free energy of all PhPhCN relative to the free energy of separate PhPhCNs in the gas-phase normalized by the surface area of the unit cell. PhPhCN surface coverage is given in units of monolayers (ML); unit cell is shown in parenthesis. The surface area of (4x4) and (6x4) unit cells is 1.05 and 1.58 nm<sup>2</sup> for Pd(111), respectively, and 1.18 and 1.76 nm<sup>2</sup> for Au(111), respectively.

Surface	Parallel		Perpendicular	
	BFE/A	Coverage	BFE/A	Coverage
$\frac{1}{4}$ ML O-precovered Pd(111)	-1.01	$\frac{1}{12}$ (6x4)	<b>-3.21</b>	$\frac{1}{4}$ (4x4)
$\frac{1}{2}$ ML Cl-precovered Pd(111)	<b>-1.04</b>	$\frac{1}{12}$ (6x4)	-0.73	$\frac{1}{4}$ (4x4)
$\frac{1}{4}$ ML O-precovered 1 ML Pd on Au(111)	-1.06	$\frac{1}{12}$ (6x4)	<b>-2.66</b>	$\frac{1}{4}$ (4x4)
$\frac{1}{2}$ ML Cl-precovered 1 ML Pd on Au(111)	<b>-0.96</b>	$\frac{1}{12}$ (6x4)	-0.76	$\frac{1}{4}$ (4x4)
$\frac{1}{4}$ ML O-precovered $\frac{1}{8}$ ML Pd on Au(111)	-1.22	$\frac{1}{12}$ (6x4)	<b>-1.39</b>	$\frac{1}{4}$ (4x4)
$\frac{1}{2}$ ML Cl-precovered $\frac{1}{8}$ ML Pd on Au(111)	<b>-0.92</b>	$\frac{1}{12}$ (6x4)	-0.58	$\frac{1}{4}$ (4x4)
$\frac{1}{16}$ ML Pd on Au(111)	<b>-0.91</b>	$\frac{1}{16}$ (4x4)	-0.86	$\frac{1}{4}$ (4x4)
$\frac{1}{2}$ ML Cl-precovered $\frac{1}{16}$ ML Pd on Au(111)	<b>-0.79</b>	$\frac{1}{16}$ (4x4)	-0.47	$\frac{1}{4}$ (4x4)
Clean Au(111)	<b>-1.19</b>	$\frac{1}{12}$ (6x4)	-0.10	$\frac{1}{4}$ (4x4)
$\frac{1}{2}$ ML Cl-precovered Au(111)	<b>-0.93</b>	$\frac{1}{12}$ (6x4)	-0.07	$\frac{1}{4}$ (4x4)

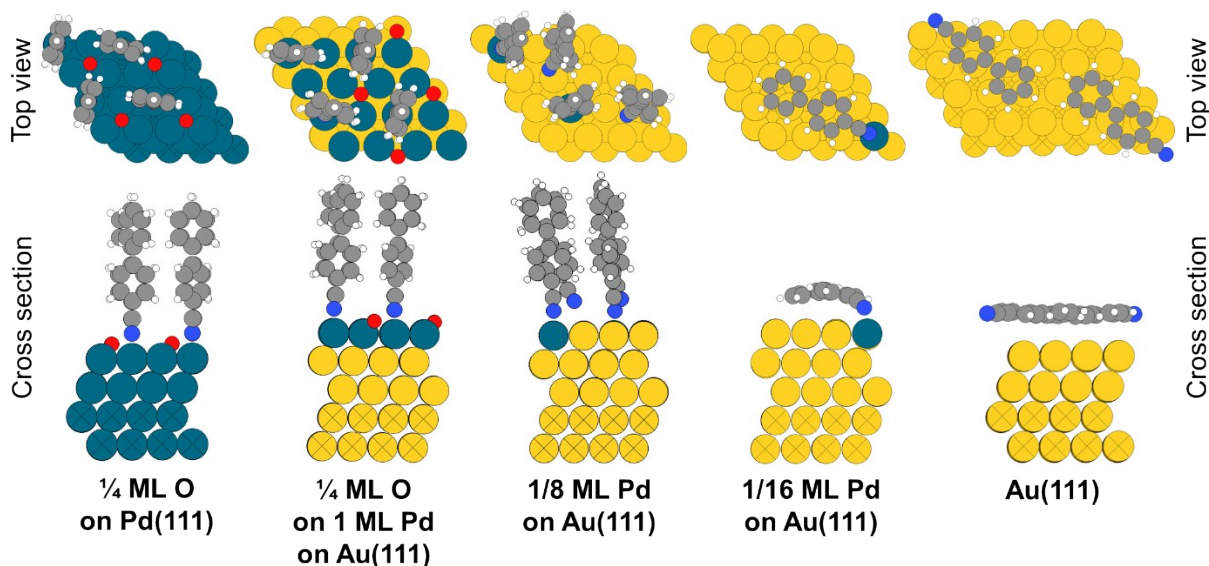


**Figure S2.** Top view (top row) and cross section (bottom row) showing the preferred orientation of PhPhCN for computational models under experimentally relevant conditions (1 atm air, 298 K), from left to right:  $\frac{1}{4}$  ML O-precovered Pd(111),  $\frac{1}{4}$  ML O-precovered 1 ML Pd on Au(111),  $\frac{1}{8}$  ML Pd on Au(111),  $\frac{1}{16}$  ML Pd on Au(111), and Au(111). Red, blue, grey, white, cyan, and yellow circles indicate O, N, C, H, Pd, and Au atoms, respectively. Crossed atoms were not allowed to relax during energy minimization.

Figure S2 shows the preferred orientation of PhPhCN on different slab models. Corresponding energetics based on BFE/A are provided in Table S1. We find that PhPhCN prefers the perpendicular orientation in the case of  $\frac{1}{4}$  ML O-precovered Pd(111) and the  $\frac{1}{4}$  ML O-precovered 1 ML Pd on Au(111). The respective calculated BFE/A (Table S1) is  $-3.21$  and  $-2.66$  eV/nm<sup>2</sup>, whereas parallel states are much less stable ( $-1.01$  and  $-1.06$  eV/nm<sup>2</sup>, respectively). This strong binding of PhPhCN is due to the nitrile group's preference to bind to the top of Pd atoms. PhPhCN molecules that cannot bind to Pd atoms, due to the limited availability of surface Pd atoms, try to adopt a planar orientation in adjacent Au atoms, because planar orientation is preferred on Au(111). However, planar orientation requires a large surface area, which is not present due to the existence of perpendicular PhPhCN molecules that are strongly bound to Pd atoms through dative bonds. As a result, PhPhCN molecules that cannot bind to Pd still have to orient perpendicular to the surface due to steric hindrance. However, because they are above Au atoms, which do not bind the N of CN as strongly as Pd atoms do, the PhPhCN molecules rise further away from the surface plane (N-Pd distance is 2.058 Å whereas the N-Au distance is 3.053 Å). Thus, the favored vertical alignment suggests that the interaction of the CN with Pd is the strongest interaction that governs the overall orientation, neighbor interactions between adjacent PhPhCNs are only of secondary importance as far as determining the vertical positioning of PhPhCN molecules. Exploratory calculations have showed that the nitrile group does not bind to the hollow or bridge sites; these are not stable structures. To rationalize the strong binding of the nitrile group of PhPhCN, we calculate electron density difference plots for the  $\frac{1}{4}$  ML O precovered Pd(111) model (Figure S3). We find large charge transfer, shown by the extended charge accumulation and depletion regions, between the nitrile group and the  $d_z^2$  orbital of Pd. The plot also explains why the top site is exclusively preferred by the nitrile group; the  $d_z^2$  orbital points to the top of the Pd atom, thus, interaction with this orbital is prohibited at other surface sites. To support the difference in reactivity of bimetallic and Pd-dominated surface, we calculated the d-band center of a surface Pd atom in the two models, which is characteristic of Pd's reactivity in the two distinct surface environments. Specifically, we found that the d-band center of Pd is  $-1.43$  eV (below the Fermi

level) for 0.09 ML Pd in Au(111) while it is -1.26 eV for 1 ML Pd on Au(111), clearly pointing to the stronger binding of the nitrile group on the 1 ML Pd on Au(111) surface. The latter is a reasonable representation of the 1.8 ML Pd on Au system, i.e.: the Pd-dominated surface. Importantly, BFE/A indicates that PhPhCN prefers planar orientation for Au(111): -1.19 eV/nm<sup>2</sup> for planar versus -0.10 eV/nm<sup>2</sup> for perpendicular orientation. Because Au is inert, binding of the nitrile group is weak and dispersion interaction between the phenyl rings and the surface provide stronger binding.<sup>26</sup> Finally, we analyze PhPhCN binding on the 1/8 and 1/16 ML Pd on Au(111). Interestingly, BFE/A suggests very similar values for perpendicular and parallel orientations (Table S1) but with opposite preference for 1/8 and 1/16 ML Pd on Au(111). 1/8 ML Pd on Au(111) prefers perpendicular orientation (-1.39 eV/nm<sup>2</sup>) while 1/16 ML Pd on Au(111) favors parallel orientation (-1.18 eV/nm<sup>2</sup>). This suggests that the transition from perpendicular to parallel orientation of PhPhCN takes place in between 1/8 and 1/16 ML Pd on Au(111). Therefore, we conclude that the computational models indicate that even a few Pd atoms in the dilute alloy limit can be sufficient to tune the orientation of 5CB.

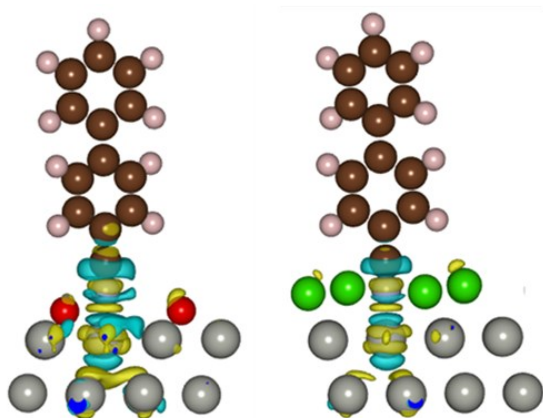


**Figure S3.** Electron density difference plot to analyze the binding of PhPhCN on  $\frac{1}{4}$  ML O-precovered Pd(111) (left) and  $\frac{1}{2}$  ML Cl-precovered Pd(111) (right). Cyan and yellow regions indicate electron-density depletion and accumulation, respectively. Red, light blue, brown, white, green, and grey circles indicate O, N, C, H, Cl, and Pd atoms, respectively.

## Experimental Characterization

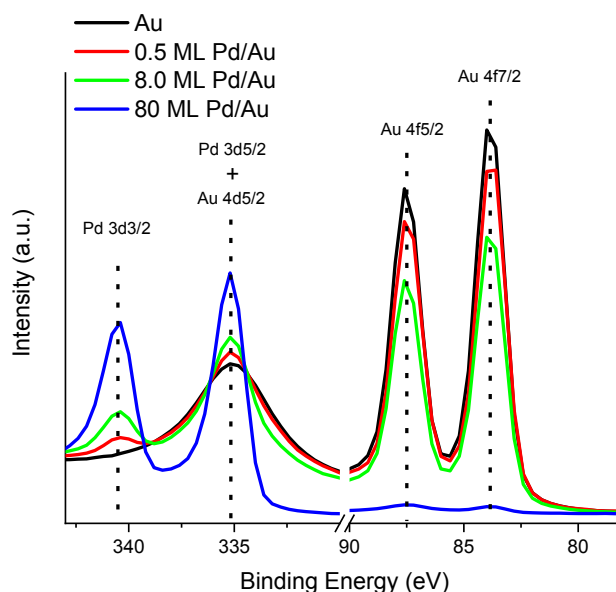


**Figure S4.** XPS showing Pd and Au peaks for different thicknesses of Pd deposited on Au.

## Cl Binding on Model Surfaces

To further verify the computational prediction that the homeotropic orientation of 5CB on PdAu alloy surfaces is due to the binding of the nitrile group to Pd atoms, we sought to disrupt the binding by introducing  $\text{Cl}_2$  into the system. Cl atoms generated by the dissociative adsorption of  $\text{Cl}_2$  bind strongly on metal surfaces<sup>27-29</sup> and would, we predicted, displace pre-adsorbed 5CB molecules.

First, we calculated the interaction of  $\text{Cl}_2$  with all previously described computational models in the presence of the PhPhCN in its favored orientation. We found that despite the high surface coverage of PhPhCN and O,  $\text{Cl}_2$  can still dissociatively adsorb in all cases. Therefore, we concluded that all  $\text{Cl}_2$  molecules diffusing towards the surface will bind to it regardless of which of the two metals, Au or Pd, is present on the surface. As a next step, we assessed surface coverages at realistic experimental conditions. To achieve this, we refer to the phase diagram we constructed previously for Au(111), which showed that  $\frac{1}{2}$  ML Cl-coverage can be found (Figure S5) without surface reconstruction at experimentally relevant conditions (1 ppm  $\text{Cl}_2$  at ambient).<sup>26</sup> Surface reconstruction will likely result in even higher Cl coverages as surface science experiments indicate<sup>30</sup>. However, we exclude surface reconstruction from our considerations for the sake of simplicity.

To determine realistic Cl-coverages on Pd containing model surfaces, we first calculated the BFE/A for  $\frac{1}{2}$  ML Cl coverage on Pd(111) to be  $-11.38$  eV/nm<sup>2</sup>. BFE/A shows stronger overall binding of  $\frac{1}{2}$  ML Cl coverage on Pd(111) compared to Au(111) for which the BFE/A is  $-7.12$  eV/nm<sup>2</sup>. As a comparison, we also calculated the BFE/A of  $\frac{1}{4}$  ML O coverage on Pd(111) to be  $-5.20$  eV/nm<sup>2</sup>. Therefore, we suggest that  $\frac{1}{2}$  ML Cl-coverage can be reached on Pd(111) even if Pd(111) was oxidized ( $\frac{1}{4}$  ML O-coverage) prior to being exposed to  $\text{Cl}_2(\text{g})$ . Thus, we conclude that Cl coverage of  $\frac{1}{2}$  ML for each model is a realistic estimate to be adopted for this study (Figure S5).

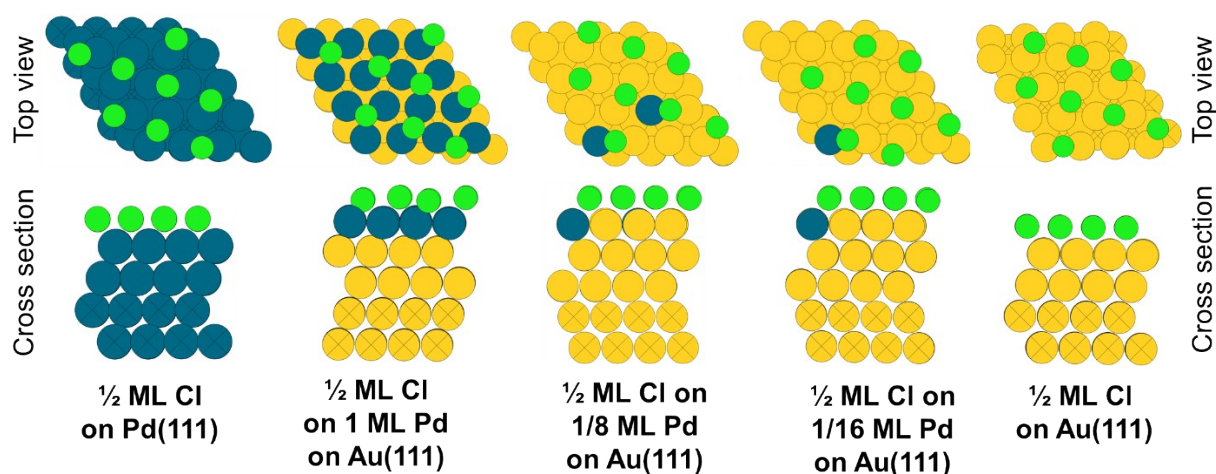


**Figure S5.** Top view (top row) and cross section (bottom row) for the computational models under experimentally relevant conditions upon exposure to 1 ppm  $\text{Cl}_2$  (1 atm air, 298 K), from left to right:  $\frac{1}{2}$  ML Cl-precovered Pd(111),  $\frac{1}{2}$  ML Cl-precovered 1 ML Pd on Au(111),  $\frac{1}{2}$  ML Cl-precovered  $\frac{1}{8}$  ML Pd on Au(111),  $\frac{1}{2}$  ML Cl-precovered  $\frac{1}{16}$  ML Pd on Au(111), and  $\frac{1}{2}$  ML Cl-precovered Au(111). Green, cyan, and yellow circles indicate Cl, Pd, and Au atoms, respectively. Crossed atoms were kept fixed during energy minimization.

## Binding of PhPhCN on Cl-covered Model Surfaces

Figure S6 shows the preferred orientation of PhPhCN on  $\frac{1}{2}$  ML Cl-precovered slab models. Corresponding energetics based on BFE/A is provided in Table S1. We find that the parallel orientation of PhPhCN is preferred for all these surfaces (Table S1). For (6x4) unit cells, the arrangement of the Cl atoms is considerably different than that of the (4x4) unit cells for all models because the most favorable arrangements for  $\frac{1}{2}$  ML Cl coverage in the (4x4) unit cells are not present in (6x4) unit cells (Figure S6). Because the interaction between the surface and the PhPhCN layer is based on weak dispersion interactions, the complex arrangements of the Cl coverage in (6x4) unit cells does not play significant role in the strength of the PhPhCN-surface interactions.

In summary, our computational analysis suggests that exposure of these surfaces to  $\text{Cl}_2$  leads to a high atomic Cl coverage, which in turn disrupts the PhPhCN bond with the surface, leading to an optical transition from homeotropic to planar anchoring of 5CB observed in experiments. To rationalize this conclusion further, we calculate the electron density difference plot for PhPhCN binding in perpendicular orientation for  $\frac{1}{2}$  ML Cl-covered Pd(111) (Figure S3) and compare it to its binding on a  $\frac{1}{4}$  ML O-covered Pd(111). We find that there is smaller charge transfer between the nitrile group of PhPhCN and the surface in the case of Cl-presence, indicating that perpendicular PhPhCN binding is much weaker on the  $\frac{1}{2}$  ML Cl-precovered Pd(111) than it is on the  $\frac{1}{4}$  ML O-precovered Pd(111) surface.

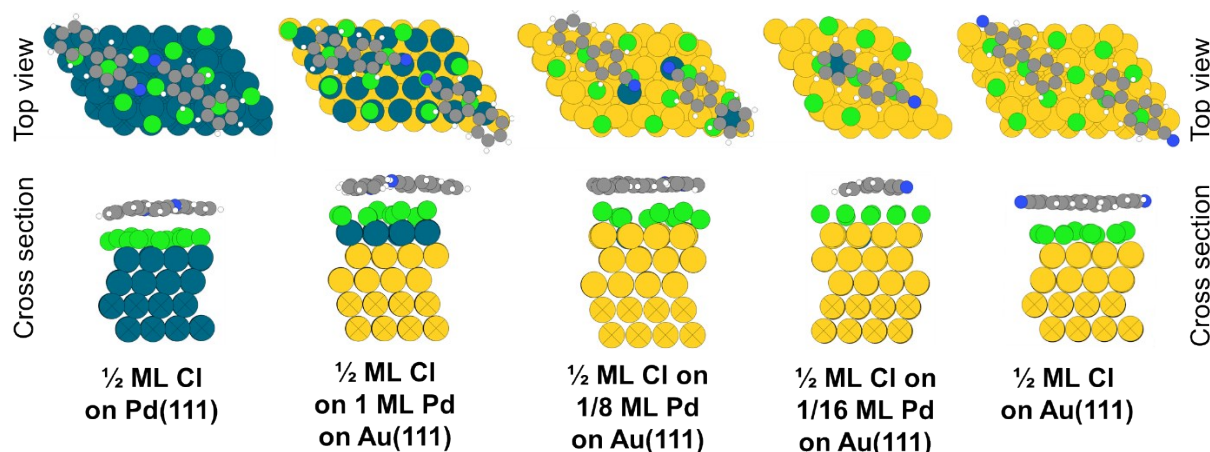


**Figure S6.** Top view (top row) and cross section (bottom row) showing the preferred orientation of PhPhCN for computational models under experimentally relevant conditions upon exposure to 1 ppm  $\text{Cl}_2$  (1 atm air, 298 K), from left to right:  $\frac{1}{2}$  ML Cl-precovered Pd(111),  $\frac{1}{2}$  ML Cl-precovered 1 ML Pd on Au(111),  $\frac{1}{2}$  ML Cl-precovered  $\frac{1}{8}$  ML Pd on Au(111),  $\frac{1}{2}$  ML Cl-precovered  $\frac{1}{16}$  ML Pd on Au(111), and  $\frac{1}{2}$  ML Cl-precovered Au(111). Green, blue, grey, white, cyan, and yellow circles indicate Cl, N, C, H, Pd, and Au atoms, respectively. Crossed atoms were kept fixed during energy minimization.

## Experimental Characterization of Chemoresponse

We performed several control experiments to confirm that the optical response of 5CB shown in Figure 3b was triggered by dissociative adsorption of  $\text{Cl}_2$  on the surface of Pd/Au film. Because  $\text{Cl}_2$  is a strong oxidizing agent, we considered the possibility that Cl oxidizes 5CB and leads to the optical transition shown in Figure 3c. However, we measured the nematic-to-isotropic transition temperature ( $T_{\text{NI}}$ ) of 5CB before and after exposure to 1 ppm  $\text{Cl}_2$  for 2 hours, a time scale that is well beyond the chemoresponse reported in Figure 3d and observed that  $T_{\text{NI}}$

of 5CB did not change (35.5 °C). Two additional control experiments were performed to minimize the possibility that the response in Figure 3b was due to a reaction between Cl<sub>2</sub> and the bulk 5CB: (i) we exposed 5CB to 1ppm Cl<sub>2</sub> gas for 2 hours. Subsequently, the 5CB was placed on 0.09±0.02 ML Pd/Au surfaces. We observed a homeotropic orientation (Figure S3a), which subsequently could be triggered to a planar orientation by Cl<sub>2</sub> (Figure S3b), and (ii) 5CB was placed onto 0.09±0.02 ML Pd/Au surfaces which were exposed to 1 ppm Cl<sub>2</sub> and found to exhibit a planar orientation (Figure S3c).

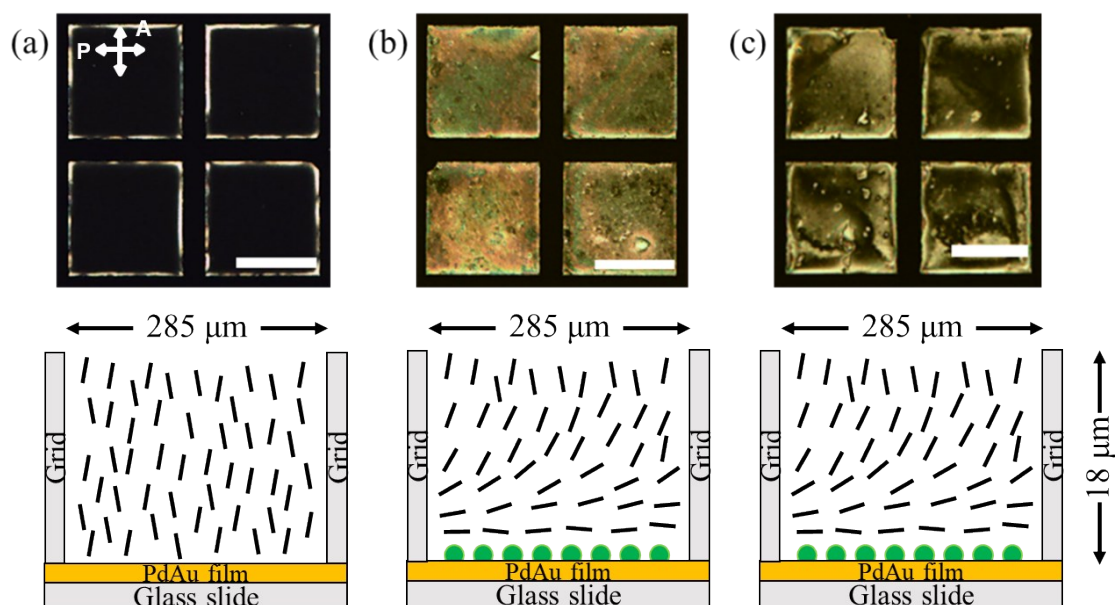


**Figure S7.** Optical micrographs (crossed polars) of Cl<sub>2</sub>-exposed 5CB supported on 0.09±0.02 ML Pd on Au surface (a) initial state, (b) exposed to 1 ppm of Cl<sub>2</sub> for 15 mins, and (c) 5CB supported on Cl-adsorbed 0.09±0.02 ML Pd on Au surface. A schematic representation of the LCs is shown to the bottom of each optical image. Black lines indicate the director of LCs. Green circles represent Cl atoms. Scale bar: 200 μm.

## Transport Model

To better describe the dynamic response of 5CB to different concentrations of Cl<sub>2</sub>, we developed a transport model according to past studies<sup>17,31</sup>, which assumes Cl<sub>2</sub> immediately reacts upon arrival (via diffusion) at the PdAu surfaces. This assumption is motivated by our DFT calculations (see above) suggesting that Cl<sub>2</sub> dissociation is spontaneous on all PdAu surfaces even if they are pre-covered with ¼ ML PhPhCN. A schematic diagram of the concentration profile of Cl<sub>2</sub> is shown in Figure S8. Cl<sub>2</sub> diffuses through a vapor phase boundary layer and subsequently a LC film with thickness δ<sub>N<sub>2</sub></sub> and δ<sub>LC</sub> (thickness of TEM grid, 20 μm), respectively. The calculation of the boundary layer thickness, δ<sub>N<sub>2</sub></sub> (in cm), was calculated to be 0.26 cm using Equation S1, which was developed for mass transfer over flat plates in laminar flow.<sup>32</sup>

$$\delta_{N_2} = 3.0 \left( \frac{x}{U_\infty} \right)^{\frac{1}{2}} \left( 1 - \left( \frac{x_0}{x} \right)^{\frac{3}{4}} \right)^{\frac{1}{3}} (v_G)^{\frac{1}{6}} (D_{N_2})^{\frac{1}{3}}$$

S1

The value of  $x$  is 0.64 cm, which represents the horizontal distance from the edge of substrate glass to the center of the TEM grid, and  $x_0$  (0.15 cm) is the horizontal distance from the edge of TEM grid to the center of the TEM grid.  $U_\infty$  is the velocity of the gas stream, which is 0.0694 m/s for the gas volumetric flow of  $V = 1000$  mL/min. We calculate the gas velocity from the

cross-sectional area (A)  $U_\infty = V/A$ . The cross-sectional area of the cell is  $A = 4 \times 0.6 \text{ cm}^2$ .  $\nu_G$  is the kinematic viscosity of  $N_2$ , which is 15.3 cSt at 20 °C.

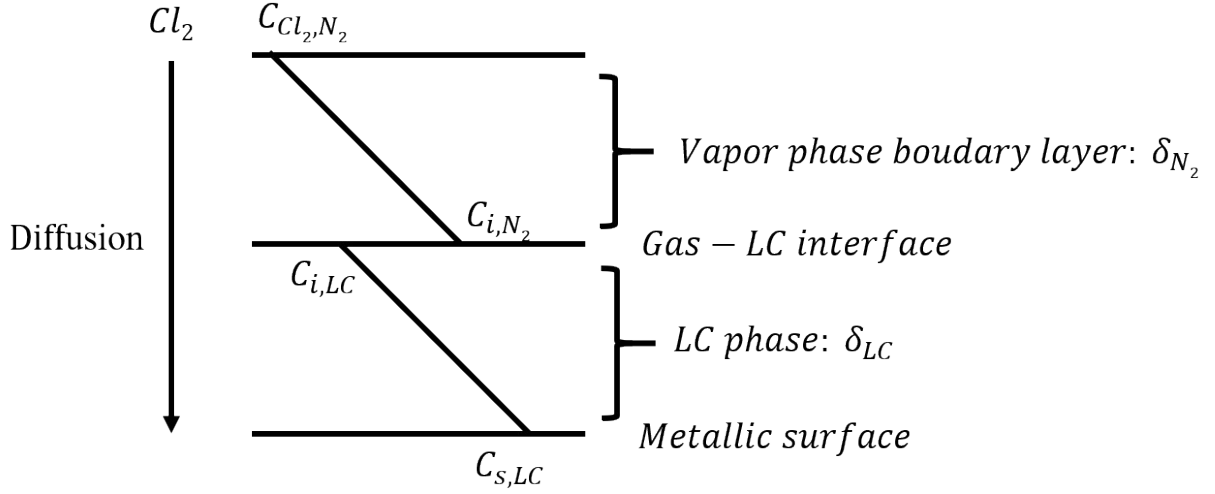


**Figure S8.** Schematic illustration of the concentration profile of  $Cl_2$  as  $Cl_2$  diffuses from the gas-phase (top) to the PdAu metallic surface (bottom).

We assumed that  $Cl_2$  is in equilibrium at the LC-air interface. The concentration of  $Cl_2$  on the vapor side ( $C_{i,N_2}$ ) and LC side ( $C_{i,LC}$ ) can be connected by partition coefficient (H):  $C_{i,LC} = C_{i,N_2}/H$ . The partition coefficient of  $Cl_2$  at the  $N_2$ -LC interface is calculated to be 0.24 (mol/volume) by all-atom force field molecular dynamics (MD) simulation (i.e.:  $Cl_2$  prefers to be in the LC than in  $N_2$ ).<sup>31</sup>

To derive a transport-reaction model, we first define the flux of  $Cl_2$  across the  $N_2$  ( $N_{N_2}$ ) and LC phase ( $N_{LC}$ ) in Equation S2 and Equation S3, respectively, assuming Fick's law of diffusion.

$$N_{Cl_2 \text{ in } N_2} = -\frac{D_{N_2}}{\delta_{N_2}}(C_{i,N_2} - C_{B,N_2}) \quad S2$$

$$N_{Cl_2 \text{ in } LC} = -\frac{D_{LC}}{\delta_{LC}}(C_{s,LC} - C_{i,LC}) = -\frac{D_{LC}}{\delta_{LC}}\left(C_{s,LC} - \frac{C_{i,N_2}}{H}\right) \quad S3$$

The flux on the vapor side depends on the diffusion constant of  $Cl_2$  in  $N_2$  ( $D_{N_2}$ ), boundary layer thickness ( $\delta_{N_2}$ ), and the concentration of  $Cl_2$  in the bulk ( $C_{B,N_2}$ ) and at the  $N_2$ -LC interface ( $C_{i,N_2}$ ).  $D_{N_2}$  is calculated to be 0.13  $\text{cm}^2/\text{s}$  using Equation S4 ( $D_{AB}$  refers to diffusion of gas species A in gas species B):

$$D_{AB} = \frac{10^{-3} T^{1.75} \left( \frac{1}{M_A} + \frac{1}{M_B} \right)^{\frac{1}{2}}}{P \left[ \left( \sum V_A \right)^{\frac{1}{3}} + \left( \sum V_B \right)^{\frac{1}{3}} \right]^2} \quad S4$$

where  $V_A$  is the special diffusion parameters to be summed over atoms, groups, and structures for compound A and B. For  $Cl_2$  diffusion in  $N_2$ ,  $\sum V_{Cl_2} = 39$ , and  $\sum V_{N_2} = 20.1$ .<sup>33</sup> The total pressure (P) is 1 atm. The temperature T is 298 K.  $M_A$  and  $M_B$  are the molecular weight for compound A and B. For  $Cl_2$  diffusion in  $N_2$ ,  $M_{Cl_2} = 70.91 \text{ g/mol}$ , and  $M_{N_2} = 28 \text{ g/mol}$ .

Similarly, the flux through the LC film depends on the diffusion constant of the analyte in the LC ( $D_{LC}$ ), LC thickness ( $\delta_{LC}$ ), and the concentration of the  $Cl_2$  at the surface ( $C_{s,LC}$ ) and at the LC- $N_2$  interface ( $C_{i,LC}$ ). The diffusion constant of  $Cl_2$  in the LC phase is approximated by the MD simulations performed for 5CB along the director vector parallel to the LC (130.96  $\mu\text{m}^2/\text{s}$  for  $Cl_2$ ).<sup>31</sup>

Next, we defined the  $Cl_2$  consumption rate as:

$$R_{rxn} = \frac{dn_{Cl_2}}{Adt} = \frac{dn_{Cl}}{2Adt} = \frac{n_{Pd}d\theta_{Cl}}{2Adt} = \frac{S_{Pd}d\theta_{Cl}}{2dt} \quad S5$$

In Equation S5, we define the reaction rate as being equal to the derivative of moles of Cl<sub>2</sub> (n<sub>Cl2</sub>), which is half of the derivative of moles of atomic Cl (n<sub>Cl</sub>), with respect to time divided by area. The derivative of moles of Cl can be equal to the derivative of fraction of Pd covered by the Cl (θ<sub>Cl</sub>) multiplied by number of moles of Pd (n<sub>Pd</sub>). The ratio of n<sub>Pd</sub> with corresponding surface area (A) is defined as surface density of Pd (S<sub>Pd</sub>). We estimate S<sub>Pd</sub> from a DFT derived lattice constant for Pd.

If we assume pseudo-steady concentration profiles, then the flux (N) of Cl<sub>2</sub> in the N<sub>2</sub> and LC phase and the reaction rate must be equal as described in Equation S6. Based on the assumption that Cl<sub>2</sub> immediately reacts when it diffuses to the PdAu surfaces, C<sub>S,LC</sub> can be assumed to be 0. Therefore, by solving the combination of Equation S2, S3, S5, S6, we derive Equation S7, where K<sub>G</sub> is defined in Equation S8 as the overall mass transfer coefficient. We can integrate the expression in Equation S5 and derive Equation S7 by assuming that the response time (t<sub>r</sub>) occurs when a threshold coverage of Cl adsorbs to Pd (θ<sub>th</sub>).

$$N_{Cl_2 \text{ in } N_2} = N_{Cl_2 \text{ in } LC} = R_{rxn} \quad S6$$

$$\frac{d\theta_{Cl}}{dt} = \frac{2K_G C_{B,N_2}}{S_{Pd}} \quad S7$$

$$K_G = 1/\left(\frac{\delta_{N_2}}{D_{N_2}} + \frac{H\delta_{LC}}{D_{LC}}\right) \quad S8$$

$$\int_0^{\theta_{th}} d\theta_{Cl} = \int_0^{t_r} \frac{2K_G C_{B,N_2}}{S_{Pd}} dt \quad S9$$

$$t_r = \frac{S_{Pd}\theta_{th}}{2K_G C_{B,N_2}} \quad S10$$

The resulting Equation S10 is only part of the total transport time. We must also include the entrance time (t<sub>en</sub>) for Cl<sub>2</sub> to travel from the gas cylinder to the LC cell, and diffusion time for Cl<sub>2</sub> from bulk gas phase to metal surfaces, which gives Equation S11.

$$t_{total} = \frac{S_{Pd}\theta_{th}}{2K_G C_{B,N_2}} + t_{en} + \frac{\delta_{N_2}^2}{2D_{N_2}} + \frac{\delta_{LC}^2}{2D_{LC}} \quad S11$$

In Equation S11, t<sub>en</sub> can be estimated by the volume of tube and flow rate of Cl<sub>2</sub> to be 1.1s. The last two terms can be calculated to be 1.5 s based on the parameters calculated above.

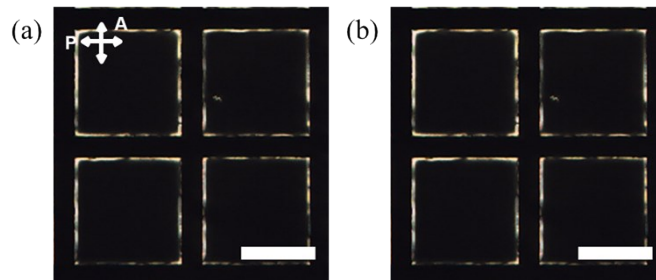


**Figure S9.** Optical micrographs (crossed polars) of N<sub>2</sub>-exposed 5CB supported on 0.09±0.02 ML Pd/Au surface (a) initial state, (b) exposed to N<sub>2</sub> with 80 % humidity for 1 hour.

### Orientation of 5CB on Au films vs Au nanoparticles

We note that some reports show homeotropic anchoring of LCs on Au nanoparticles.<sup>34,35</sup> We emphasize however that gold nanoparticles can be more reactive than e-beam deposited thick

Au films, which phenomenon is widely studied in catalysis.<sup>36</sup> Additionally, we note that there is also an early study<sup>37</sup> which also shows planar anchoring of 5CB supported on thermally evaporated Au films with 10 nm and 100 nm thickness in agreement with our previous report (ref. 14 of the manuscript). The second difference is the LC used in ref. 34 and 35. For example, ref. 34. reported vertical alignment for the thermotropic nematic LC (E31) and tangential alignment for the lyotropic chromonic LC (formed by solutions of cromolyn in de-ionized water at 13–14 wt. % to ensure a room-temperature nematic phase) while we used 5CB.

## REFERENCES

- 1 G. Kresse and J. Furthmüller, *Phys. Rev. B*, 1996, **54**, 11169.
- 2 G. Kresse and J. Furthmüller, *Comput. Mater. Sci.*, 1996, **6**, 15.
- 3 P. E. Blöchl, *Phys. Rev. B*, 1994, **50**, 17953.
- 4 G. Kresse and D. Joubert, *Phys. Rev. B*, 1999, **59**, 1758.
- 5 J. P. Perdew, K. Burke, and M. Ernzerhof, *Phys. Rev. Lett.*, 1996, **77**, 3865.
- 6 S. Grimme, J. Antony, S. Ehrlich, and H. Krieg, *J. Chem. Phys.*, 2010, **132**, 154104.
- 7 J. D. Pack and H. J. Monkhorst, *Phys. Rev. B*, 1977, **16**, 1748.
- 8 M. Methfessel and A. T. Paxton, *Phys. Rev. B*, 1989, **40**, 3616.
- 9 D. R. Lide, W. M. M. Haynes, G. Baysinger, L. I. Berger, H. V Kehiaian, D. L. Roth, D. Zwillinger, M. Frenkel, and R. N. Goldberg, *CRC Press*, 2009, **4**.
- 10 T. Szilvási, L. T. Roling, H. Yu, P. Rai, S. Choi, R. J. Twieg, M. Mavrikakis, and N. L. Abbott, *Chem. Mater.*, 2017, **29**, 3563.
- 11 L. Bengtsson, *Phys. Rev. B - Condens. Matter Mater. Phys.*, 1999, **59**, 12301.
- 12 J. T. Hunter, S. K. Pal, and N. L. Abbott, *ACS Appl. Mater. Interfaces*, 2010, **2**, 1857.
- 13 S. W. Thomas, S. J. Vella, M. D. Dickey, G. K. Kaufman, and G. M. Whitesides, *J. Am. Chem. Soc.*, 2009, **131**, 8746.
- 14 C. E. D. Chidsey, D. N. Loiacono, T. Sleator, and S. Nakahara, *Surf. Sci.*, 1988, **200**, 45.
- 15 M. Baldauf and D. M. Kolb, *Electrochim. Acta*, 1993, **38**, 2145.
- 16 J. M. ROBERTSON, *Nature*, 1944, **154**, 349.
- 17 J. T. Hunter and N. L. Abbott, *Sensors Actuators B Chem.*, 2013, **183**, 71.
- 18 F. P. Leisenberger, G. Koller, M. Sock, S. Surnev, M. G. Ramsey, F. P. Netzer, B. Klötzer, and K. Hayek, *Surf. Sci.*, 2000, **445**, 380.
- 19 V. V. Kaichev, I. P. Prosvirin, V. I. Bukhtiyarov, H. Unterhalt, G. Rupprechter, and H. J. Freund, *J. Phys. Chem. B*, 2003, **107**, 3522.
- 20 B. L. Frey, R. M. Corn, S. C. Weibel, in *Handb. Vib. Spectrosc.* (Ed.: P.R. Griffiths), John Wiley & Sons, Ltd, Chichester, UK, **2006**.
- 21 Y. Xu and M. Mavrikakis, *J. Phys. Chem. B*, 2003, **107**, 9298.
- 22 G. Zheng and E. I. Altman, *Surf. Sci.*, 2000, **462**, 151.
- 23 S. Han and C. B. Mullins, *ACS Catal.*, 2018, **8**, 3641.
- 24 E. L. Kolsbjerg, M. N. Groves, and B. Hammer, *J. Chem. Phys.*, 2016, **145**, 094107.
- 25 J. Greeley and M. Mavrikakis, *Nat. Mater.*, 2004, **3**, 810.
- 26 H. Yu, T. Szilvási, K. Wang, J. I. Gold, N. Bao, R. J. Twieg, M. Mavrikakis, and N. L. Abbott, *J. Am. Chem. Soc.*, 2019, **141**, 16003.
- 27 B. V. Andryushechkin, T. V. Pavlova, and K. N. Eltsov, *Surf. Sci. Rep.*, 2018, **73**, 83.
- 28 A. G. Shard, V. R. Dhanak, and A. Santoni, *Surf. Sci.*, 1999, **429**, 279.
- 29 Y. Santiago-Rodríguez, J. A. Herron, M. C. Curet-Arana, and M. Mavrikakis, *Surf. Sci.*, 2014, **627**, 57.
- 30 W. Gao, T. A. Baker, L. Zhou, D. S. Pinnaduwege, E. Kaxiras, and C. M. Friend, *J. Am. Chem. Soc.*, 2008, **130**, 3560.

- 31 J. K. Sheavly, J. I. Gold, M. Mavrikakis, and R. C. Van Lehn, *Mol. Syst. Des. Eng.*, 2020, **5**, 304.
- 32 J. Krenn, S. Baesch, B. Schmidt-Hansberg, M. Baunach, P. Scharfer, and W. Schabel, *Chem. Eng. Process. Process Intensif.*, 2011, **50**, 503.
- 33 E. N. Fuller, P. D. Schettler, and J. C. Giddings, *Ind. Eng. Chem.*, 1966, **58**, 18.
- 34 J. S. Evans, C. N. Beier, and I. I. Smalyukh, *J. Appl. Phys.*, 2011, **110**, 033535.
- 35 A. Choudhary, T. F. George, G. Li, *Biosensors*, 2018, **8**, 69.
- 36 N. Lopez, T. V. W. Janssens, B. S. Clausen, Y. Xu, M. Mavrikakis, T. Bligaard, and J. K. Nørskov, *J. Catal.*, 2004, **223**, 232.
- 37 P. N. Sanda, D. B. Dove, H. L. Ong, S. A. Jansen, and R. Hoffmann, *Phys. Rev. A*, 1989, **39**, 2653.